THE JOURNAL OF PHYSICAL CHEMISTRY B
A JOURNAL OF THE AMERICAN CHEMICAL SOCIETY

pubs.acs.org/JPCB Article

Side-Chain and Ring-Size Effects on Permeability in Artificial Water Channels

Tyler J. Duncan, Harekrushna Behera, Michael F. Meng, Zidan Zhang, Nico Marioni, Meron Tadesse, Manish Kumar, and Venkat Ganesan*

Cite This: J. Phys. Chem. B 2025, 129, 659−670

Read Online

ACCESS | Metrics & More | Article Recommendations | Supporting Information

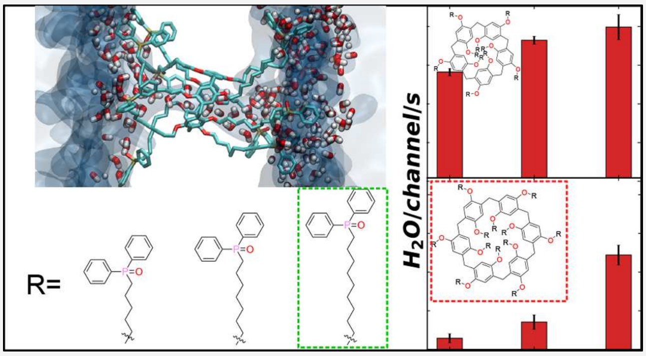

ABSTRACT: Artificial water channels (AWCs) have emerged as a promising framework for stable water permeation, with water transport rates comparable to aquaporins (3.4−40.3 × 10^8 H_2O/channel/s). In this study, we probe the influence of ring-size and side-chain length on the water permeability observed within a class of AWCs termed ligand-appended pillar[n]arenes (LAPs) that have an adjustable ring-size (m) and side-chain length (n). Through all-atom molecular dynamics simulations, we calculate the permeability of these channels using the collective diffusion model and find their permeabilities. We characterize the mechanistic influence of pillar[n]arene ring-size and side-chain length on the channel water permeability by analyzing the characteristics of the internal permeating water-wire and the surrounding channel structure. We observe that water permeability decreases as a function of increasing ring-size due to increases in hydrophilic contacts between the permeating water-wire and the oxygen groups on the channel wall. Further, we observe an increase in water permeability as a function of side-chain length due to increased partitioning of the channel terminal groups into the hydrophilic blocks of the surrounding bilayer. For the LAP6 channel, with increase in side-chain length, the distance between terminal groups increases and leads to an increase in pore size, thereby enhancing water permeability. In the case of LAP5, as side-chain length increases, the channel displays a compensatory effect between tilt and bend angle due to the flexible side-chains. Such flexibility leads to higher terminal group partitioning in the hydrophilic blocks of the bilayer and extends the permeating water-wire. This increase in water-wire length and hydrophilic block access overcomes the nonmonotonic pore size trend in pillar[5]arene channels.

1. INTRODUCTION

As freshwater scarcity spreads throughout the world, the demand for desalination membranes has increased exponentially. Such membranes have greatly improved energy costs over thermal desalination processes and are used to produce approximately 142 × 10^6 m^3/day of desalinated water.[1] However, present membranes suffer from a trade-off in which higher salt rejection is often accompanied by lower water permeabilities.[1] Emerging technologies seek to improve this permeability and reduce the overall footprint and economic weight of the desalination processes.[2] Such state of the art membranes use polyamide thin film composites (PA-TFCs) such that the water transport across the membranes is enhanced while maintaining ion rejection (>99%).[3] However, precise control over pore distribution and pore functionality have become major hurdles for maintaining ion rejection within these membranes.[4]

As an alternative to conventional polyamide membranes, an emerging class of macrocyclic molecules has been promoted as having precise pore size distributions by mimicking biological membranes.[5] The inspiration for such strategies derives from channel embedded-membranes which display high permeabilities and selectivities within biological systems.[6] For instance, aquaporins (AQPs), which are responsible for cell homeostasis, offer permeabilities of 3.4−40.3 × 10^8 H_2O/channel/s via one-dimensional water transport while promoting an astounding ion rejection of 10^9:1 H_2O:Na^+.[7] Such one-dimensional water transport, termed a water-wire, decreases the degrees of freedom for water transport and has been found to greatly enhance permeability by limiting the hydrogen bonding of water with channel walls and between water molecules.[8] While AQPs offer a tantalizing capacity for membrane desalination, the complexity of the protein assembly

Received: August 2, 2024
Revised: November 8, 2024
Accepted: December 12, 2024
Published: January 2, 2025

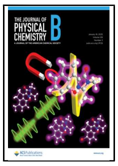

https://doi.org/10.1021/acs.jpcb.4c05244
J. Phys. Chem. B 2025, 129, 659−670

within the bilayer causes AQPs to exhibit significant thermal sensitivity and stability issues which have limited applications.[9] Carbon nanotubes (CNTs) have seemingly addressed some of AQPs' drawbacks while maintaining experimental permeabilities of 7.7×10^9 H_2O/channel/s.[10] Such CNT channels also provide an additional design parameter, viz., nanotube radii, that allows for precise size sieving of ions and small molecules.[11] However, CNTs are limited in design parameters when it comes to the appendable chemistries and length.[12]

Advances in macrocyclic chemistry have identified a number of synthetic alternatives for transmembrane ion−water separations, such as peptide-appended pillar[n]arenes (PAPs).[7] These molecules are the latest in the lineage of membrane-embedded channels and are commonly termed artificial water channels (AWCs). The synthetic architecture of AWCs make them an ideal candidate for tailor-made transmembrane separations through precise control of appended ligands (hydrophilicity, ion-channel binding, membrane-channel stability, and channel length) and pore size (number of monomers in central ring).[5] Through such tunable parameters, AWCs propose precision engineering of permeant local environments while remaining stable under thermal and pressure fluctuations. The synthetic architecture underlying AWCs has also been shown to greatly increase the stability of these channels by decoupling transmembrane conformations from the helicity found in proteins such as aquaporin (AQP) when embedded in lipid and lipid-like block copolymer bilayers.[7,13]

In the context of AWCs, early design parameters focused on constricting the channel pore size to promote fast, one-dimensional water-wires similar to those observed in highly permeable biological membranes.[7] Specifically, channel diameters approaching this angstrom-scale confinement ≈1.08 nm have been observed to present such ballistic one-dimensional transport of water while rejecting some small molecules.[8] Further extending the range of diameters for ion selectivity, pillar[n]arene can be synthesized in 5-membered and 6-membered rings with $d_{\mathrm{LAP5}} = 0.47$ and $d_{\mathrm{LAP6}} = 0.58$ nm.[14] With fast water permeability satisfied through confinement effects, ligands containing low ion and residue activity, such as triPhe peptides, were selected to mimic AQPs' ion rejection and phenylalanine-lined inner core.[15]

Pursuing these early design parameters, PAP and peptide-appended hybridene (PAH), has probed 4- and 5-membered rings with peptide-appended hybrid[4]ene (PAH[4] and PAP[5]), respectively.[7,16] Common candidates explored for these appended chemistries contain hydrophilic motifs at their termini to facilitate the formation of transmembrane conformations and provide rejection for common ions. When such motifs are present, the ligands partition favorably into the hydrophilic bilayer blocks, thus forming transmembrane pores.[17] In the case of PAH[4] and PAP[5], the insertion of the channel species was enumerated via fluorescent labeling of the appended peptide carboxylic groups which indicated that these channels have high packing ratios of 2.6×10^5 pores/μm^2.[7] In addition to high packing ratios, pillar[n]arenes form robust transmembrane conformations that surpass the stability of traditional transmembrane proteins.[7,18] The channel, PAH[4], exhibits water permeability of 8.9×10^8 H_2O/channel/s, while PAP[5] presents 3.5×10^8 H_2O/channel/s with water uptake into the channel (swelling) occurring on time scales of approximately 30 ns.[7,17] Further, PAH[4] was reported to completely exclude common ion transport even under applied potential ($\Delta E = \pm 1$ V).[16] PAP[5] presented ion selectivities in the following hierarchy $NH_4^+ > Cs^+ > Rb^+ > K^+ > Na^+ > Li^+ > Cl^-$ with a molecular weight cutoff around 500 Da.[7,15,17] With the combination of features available through the PAP and PAH channels, such AWCs have become of growing interest for separations.

Motivated by the high permeability and selectivity discovered in PAP channels, in this study, we expand the parameter space of pillar[n]arene channels, particularly membrane inserted ligand modified pillar[n]arene (LAP) channels, by probing the effects of ring-size and side-chain length on the performance of pillar[*n*]arenes appended with ionophillic motifs.[13,19] The ionophillic ligand analyzed in this study contains a terminal diphenyl phosphine oxide (DPP) which, in previous studies, has demonstrated novel actinide/lanthanide (Ac^{4+}/Ln^{3+}) binding selectivity and has been applied in rare earth element (REE) recovery efforts.[20] Since water and ion transport are usually correlated, we hypothesize that unraveling the underlying water transport characteristics may provide insight on the ion permeation of such channels.[21]

The LAP architecture, pictured in Figure 1, outlines the two parameters probed in this study. The first parameter of interest is the ring-size (m), which corresponds to the number of LAP monomers present in the channel. The second parameter of interest is the side-chain repeat unit (n), the number of bridging carbons (not counting the terminating carbons) between the ring and ligand functional group. In this study, we probe six channels comprising phase space of $n = (4, 6, 8)$ and $m = (5, 6)$. Due to the time scale for purification, synthesis, and characterization, in addition to the large parameter space for evaluation, we use molecular dynamics (MD) simulations as a means to probe our channel phase space. We first calculate single-channel permeabilities in our equilibrium MD simulations using the collective diffusion model.[22] We then seek to extract molecular-level information about the mechanisms underlying our results.

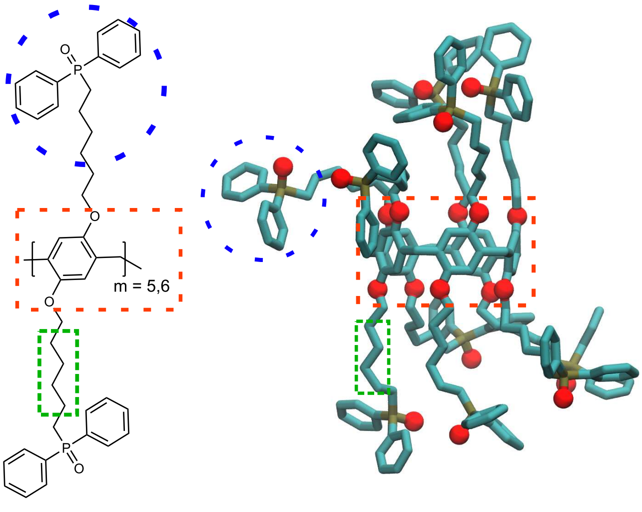

Figure 1. Scheme of ligand-appended pillar[n]ene where the backbone (ring-size: $m = 5$, 6 and side-chain length: $n = 4$, 6, 8) refers to the repeat aliphatic carbon unit in the side-chain length.

The organization of this review is as follows: We outline the simulation methods implemented in this study in Sections 2 and 3. The permeability results are presented in Section 4.1. This is followed by analysis of the internal water-wire in

Section 4.2. To understand the interactions between the permeating water and LAP channel, we probe the channel pore sizes and identify the role of the ring-size on permeability in Section 4.3. Finally, we examine the role of side-chain length in the LAP6 channel in Section 4.4 and in LAP5 in Section 4.5.

2. METHODS

2.1. Simulation Details. Simulations were conducted in the parallel MD program GROMACS 2020.2 on Lonestar 6 "Milan" CPUs containing on average 53,000 atoms.[23] These 53,000 atoms consist of 1 channel molecule, 170 1-palmitoyl-2-oleoyl-*sn*-glycero-3-phosphocholine (POCP) molecules, and 10,000 simple-point charge (SPC) water molecules.[24,25] Simulations of the channel-inserted bilayers were carried out using the density functional theory (DFT)-optimized addition to the optimized potentials for liquid simulations (OPLS) force field from Kulig et al. for the POPC bilayer.[26−28] The channel was parametrized using Jorgenson co-workers's ligand parameter generator (LigParGen) server for the LAP monomer.[29] Given the tools available for parametrizing novel molecules and availability of lipid parameters.[26,29] We selected the OPLS force field for our simulations. Studies exploring the agreement between the OPLS/AA and CHARMM force field find that OPLS/AA has low relatively standard error that arises primarily due to $\phi - \psi$ distributions, which influence simulations containing amino acids.[30−33] Bonded interactions are calculated across 1−2, 1−3, and 1−4 neighbors using harmonic bond (k_b), harmonic angle (k_θ), Ryckaert−Bellemans dihedral potential (C_n), and improper dihedrals (k_ψ), where the nonbonded interactions are weighted for f_{ij} $(i, j) = [a[1, 2], b[1, 3], c[1, 4]]$ with $[a, b, c] = [0, 0, 0.5]$.

$$U_b = \sum_b \frac{k_b}{2}(b - b_0)^2 + \sum_\theta \frac{k_\theta}{2}(\theta - \theta_0)^2 + \sum_\phi \sum_{n=0}^{5} (-1)^n C_n (\cos\phi)^n + \sum_\psi k_\psi(1 + \cos(n\psi - \psi_0)) \quad (1)$$

$$U_{nb} = \sum_{i,j} f_{ij} \left\{ \frac{e^2 z_i z_j}{4\pi\epsilon_0 r_{ij}} + \epsilon_{ij}\left[\left(\frac{\sigma_{ij}}{r_{ij}}\right)^{12} - \left(\frac{\sigma_{ij}}{r_{ij}}\right)^{6}\right]\right\} \quad (2)$$

Monomers for the LAP molecule were generated using the *Avogadro* program to initialize the channel structure.[34] Molecular topology files were generated using MKTOP to initialize OPLS atom types for the channel species and compared with the results returned from LigParGen to match to existing OPLS types.[35] Empirical charges generated from the LigParGen server for the DPP-terminal group were replaced with restrained electrostatic potential (RESP) calculations using Gaussian16 to appropriately consider the charge distribution across the phenyl and phosphate groups.[36,37] OPLS types and charges for the monomers are presented in the Supporting Information.

Following the methods outlined by Lemkul,[38] the LAP channel was relaxed and oriented in the direction of the membrane normal before insertion into the bilayer by removal of POPC molecules within 0.5−1.5 nm of the inserted channel. The first configuration of the channel was intended to place the appended ligands such that the channel orientation aligns with the membrane normal. Insertion in this configuration leads to the removal of the least number of lipids (≈27−33 lipids). Lipids around the channel are relaxed during the initial bilayer equilibration period, and strong position restraints are applied on the channel during NVT preproduction. We apply the NPT (constant **N**umber, **P**ressure, and **T**emperature) ensemble with $P = 1.0\ bar$ and $T = 323\ K$ using the Parrinello−Rahman barostat with semi-isotropic conditions and Nose−Hoover thermostat, respectively. The strong restraints applied to the channel are removed after 1 ns of simulation, and the system is returned to full-flexibility save for H-bonds handled by the LINear Constraint Solver (LINCS) algorithm.[39] The membrane simulation was solvated using the in-built GROMACS *solvate* command, and the simple-point charge (SPC) water model selected[25] was removed from the bilayer center (ranging from head-oxygen (O3) to tail carbon (C27) before beginning minimization).[38] Based on the convergence of channel root mean squared displacements (RMSD) from previous studies in POPC bilayers, production run simulations of 100 ns across 10 repeated simulations were used for analysis. We present the results for the RMSD, as shown in Figure S7.[40,41] This time was sufficient to allow for swelling within the channel to occur.[7] The SPC water model was chosen in accordance with previous bilayer studies and shows good agreement in transmembrane water transport.[25,42] The bilayer and solvent were coupled separately with the barostat and thermostat, presented above, to account for the inhomogeneity of the system.

3. ANALYSIS OF SIMULATION RESULTS

3.1. Radial Distribution Function. To quantify the structural characteristics, we probed the radial distribution function ($g(r)$) between pairs of atoms,

$$g_{ij}(r) = \frac{V}{4\pi r^2 N_i N_j} \sum_i \sum_j <\delta(r - r_{ij})> \quad (3)$$

where N_i and N_j represent the number of atoms of type *i and j* in a simulation box of size V, δ represents the Dirac delta function, and r_{ij} is the distance between the two reference atoms.

3.2. Hydrogen Bonding. To enumerate the number of hydrogen bonds between water molecules as a function of the axial coordinate, z, from the channel center, we analyze the pairwise distribution of water molecules within the system. We set the bounds for analysis where the distance between donor and acceptor oxygen is 0.35 nm and a donor hydrogen acceptor angle is less than 150°.[43,44] Water molecules with these characteristics exhibit aligned dipoles that induce the hydrogen bonding interaction.[45] Water molecules display a bulk limit of ≈3.5 H−Bond/H_2O with two donating hydrogen atoms and two accepting sites on the oxygen atom. Within the LAP chemistry, previous works have proposed that the permeating water-wire has a reduced hydrogen bonding structure.[7]

3.3. Pore Size Distribution. The radius of the channel along its length is a fundamental determinant of the solvent accessibility within the channel. To characterize such a feature, we insert a probe along the center of mass of the channel and calculate the minimum distance to the nearest atom along the channel axis (z). This minimum distance is used to identify the accessible pore size along the channel axis,

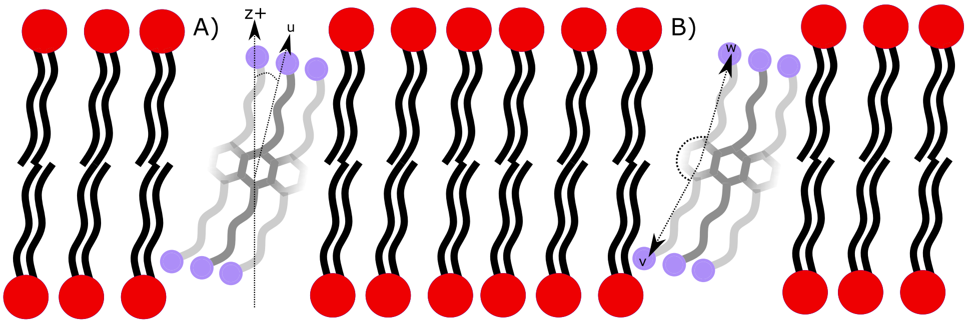

Figure 2. Idealized schematic of the channel-bilayer complex. Phosphorus headgroups (red circles) are attached onto lipids with channel molecules in the gaps. We present the vectors for calculating the orientation within the bilayer, where the tilt angle (A) is the angle between the membrane normal (+z) and the orientation of the central ring structure. Bend angle (B) presents the angle created between the terminal-DPP groups and the central ring structure.

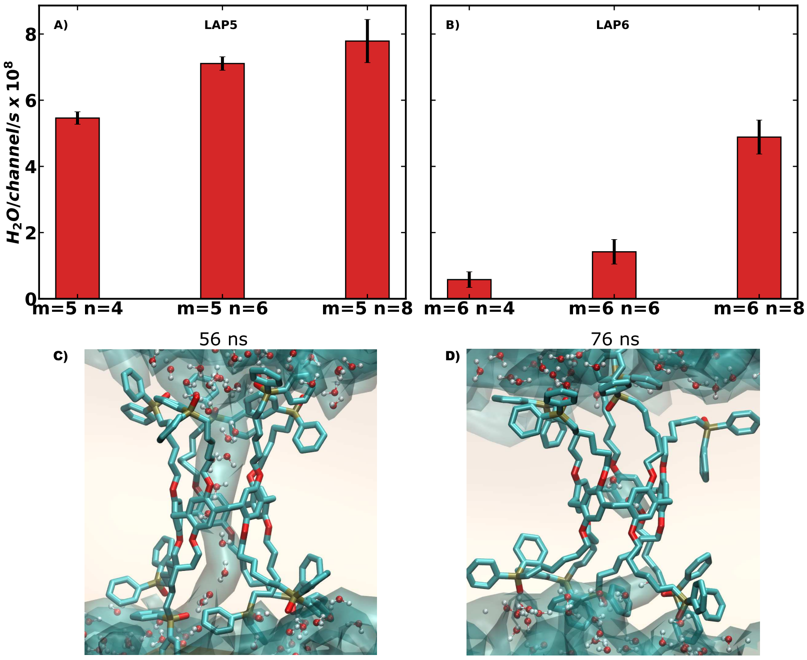

Figure 3. (A) Water dynamics in LAP5 parameter space (m = 5, n = 4, 6, 8).[22] (B) Water dynamics in LAP6 parameter space (m = 6, n = 4, 6, 8). Two snapshots of the LAP5n4 channel in the POPC bilayer at (C) 56 ns with an intact water-wire structure across the channel and (D) at 76 ns where two water molecules are bound within the channel center.

$$r(z) = \min\left\{\mathbf{R} - \frac{\sum_{\exists z_i<z<z_{i+1}} r_i m_i}{\sum_{\exists z_i<z<z_{i+1}} m_i}\right\} \tag{4}$$

where **R** is a matrix of atom positions in the molecule.

3.4. Radius of Gyration. To characterize the conformations of the channels, we calculated the radius of gyration (R_g),

$$R_g = \left(\frac{\sum_i \|\mathbf{r_i}\|^2 m_i}{\sum_i m_i}\right)^{(0.5)} \tag{5}$$

where ($\mathbf{r_i}$) is the distance of particle i from the center of mass of all atoms in the molecule and (m_i) is the mass of atom i. Since our molecule is oriented along the z-axis, we also consider the distribution in the xy-plane to analyze the molecular distribution around the z-axis.

$$R_{g_{xy}} = \left(\frac{\sum_i \left\|x_i^2 + y_i^2\right\|^2 m_i}{\sum_i m_i}\right)^{(0.5)} \tag{6}$$

3.5. Bend and Tilt Angle of Channel. In Figure 2A, we present the scheme by which the orientations of the central ring (hexagon) structure and terminal-DPP (blue) groups are used to calculate the alignment of the LAP channels relative to the lipid membrane (red) normal. Coordinates are loaded in using *MDAnalysis*.[43,44]

For calculating the tilt angle, we take a reference atom within the channel central ring and establish the plane of the central ring. We calculate the angle between the resulting vectors using

$$\theta = \mathrm{arcos}\left(\frac{\mathbf{u}\cdot\mathbf{z}+}{|\mathbf{u}||\mathbf{z}+|}\right) \tag{7}$$

where ($\mathbf{u}$) is the normal vector to the plane of the central ring and ($\mathbf{z}+$ = <**0**,**0**,**1**>) is the membrane normal vector. Tilt angle

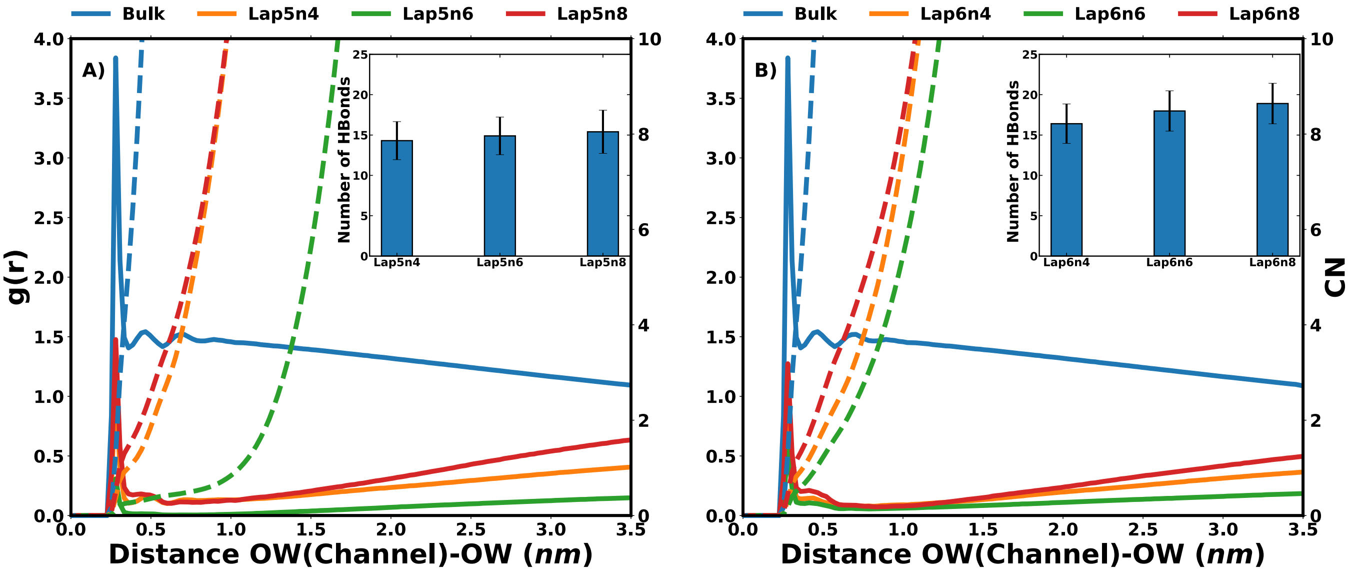

Figure 4. Radial distribution profiles $g(r)$ (solid) and coordination number (CN) (dashed) between water molecules within the (A) LAP5 and (B) LAP6 channel such that they satisfy the structure factor $|z| < L_{\text{channel}}$. (*Inset*) Enumerates the number of hydrogen bonds between the water-wire and the (A) LAP5 channel and (B) LAP6 channel wall.

has been widely employed in transmembrane protein systems to characterize channel stability in lipid membranes.[18]

For calculating the bend angle (ω), we take the two vectors **w** and **v** in Figure 2B, with the vector (**w**) representing the vector from the channel center of mass to the terminal groups in the + z direction and (**v**) denotes the vector from the channel center of mass to the terminal groups in the − z direction,

$$\omega = \arccos\left(\frac{\mathbf{w}\cdot\mathbf{v}}{|\mathbf{w}||\mathbf{v}|}\right) \tag{8}$$

Using such vectors, we obtain the bend angle as a representation of the side-chain orientation around our central macrocycle.

3.6. Single-Channel Water Permeability.

To calculate the water permeability of channels at equilibrium, we turn to the collective diffusion model.[22] This framework allows extraction of the osmotic permeability of a nanochannel in terms of H_2O/channel/s and can be directly compared with experimental measurements.[46] This method relies on the computation of the cumulative, normalized displacement of water in the nanochannel, dn. To obtain the number of water crossings in the channel, we consider the water molecules inside the channel and probe the one-dimensional displacement within the nanochannel.

$$\mathrm{d}n = \sum_{\exists |z| < L_{\text{channel}}} \mathrm{d}z_i / L_{\text{channel}} \tag{9}$$

where the summation is over the particles within the channel at time, t. The term dz_i represents the displacement of the permeant, water in this case, in the z-direction between frames spaced by 20 ps and is normalized by the length of the channel, L_{channel}. We select a bin size of L_{channel} = 1.0 nm in the z-direction across the central macrocycle such that the displacement of waters within the region z = −0.5 to 0.5 nm is calculated.[40] From this profile, we obtain a normalized velocity of the permeant across the channel. By integrating to obtain $n(t)$ with the initial condition $n(t = 0) = 0$, we get a cumulative count of the number of transport events. Taking the least-squares fit of this cumulative profile, we calculate the average water displacement when transporting across LAP5 and LAP6 channels.

4. RESULTS AND DISCUSSION

4.1. Water Transport in LAP5 and LAP6.

Figure 3 presents results for water transport rates based on 10 replicate, 100 ns simulations across our parameter space (m = 5, 6 n = 4, 6, and 8). In a comparison of Figure 3A to B, we observe a reduced permeability in the LAP6 channels relative to that of LAP5. However, we observe a monotonic increase in the permeability as the side-chain length increases ($P_{n=4} < P_{n=6} < P_{n=8}$). Together, these results suggest that the ring-size and side-chain lengths have opposite effects on the channel's water permeability. Overall, LAP5n8 is seen to present the highest permeability out of our sampled channels ($P_{\text{LAP5n8}} = 7.79 \pm 0.65 \times 10^8$ H_2O/channel/s). Our results above also suggest that the LAP framework transports water at rates comparable to that of AQPs while significantly reducing the complexity of the transmembrane chemistry.[6] From the snapshots in Figure 3C,D, we observe the formation of a single- water-wire across the transmembrane channel. We observed two separate states within these snapshots in which the transporting water molecules connect to the bulk water in a one-dimensional hydrogen bonding structure and another where waters are bound to the channel center.

To better understand the influence of the ring-size and side-chain length on LAP water permeability, we turn back to the all-atom simulations. Simulations provide atomistic insight into the structure of the internal water-wire (necessary for fast water permeation found in AQP and CNTs), the pore availability along the channel (a good measure for the water-wire environment and how the channel opens and closes), and, last, the orientation of the channel and its side-chains within the bilayer (a description of the channel stability and transmembrane conformation). We hypothesize that using such characteristics, we can rationalize the trends for water permeabilities.

4.2. 1D Water-Wire Structure. Past studies in biological protein channels have shown that the structure and interactions within the water-wire and with the surrounding channel are responsible for the one-dimensional shape, ballistic movement, and hydrogen bond alignment of the water-wire.[17,18] Within AWCs, these permeating water-wires display weak hydrogen bonded water-wires, fast transport along hydrophobic walls, supramolecular water-wires, or hydrogen bonded networks between regularly spaced functional groups.[47] Permeability within such channels is typically inversely related to the number of hydrophilic contacts the water-wire makes with the channel.[48] In this section, we present results for the structure of the innerchannel water-wire to understand the underlying permeability mechanisms of the LAP channels.

We probed the variations in hydrogen bonding contacts along the water-wire and the interactions of the water molecules with the surrounding channel with varying ring-size (m = 5, 6) and side-chain length (n = 4, 6, 8). To characterize the water structure in the LAP channels, in Figure 4A,B, we present $g(r)$ of water-oxygens within the channel ($g(r)_{\mathrm{H_2O-H_2O}}$). The first peak in $g(r)_{\mathrm{H_2O-H_2O}}$ is seen to be at the same location (0.275 nm) for both LAP5 and LAP6. The relative intensity of this peak, for both LAP5 and LAP6, is smaller than that seen in bulk water ($g_{\mathrm{bulk}}(r = 0.275\ \mathrm{nm}) \approx 4$). As a result, the coordination number (CN) profile indicates that water molecules within the channel coordinate with approximately 2 other water molecules following this first peak. LAP5n6 displays a slightly lower coordination, which suggests that permeating water molecules are coordinated to one other water when passing through the channel. Contrasting the in-channel coordination to the bulk coordination in Figure 4, in the latter, we observe each water coordinating to ≈6 neighboring water molecules following the first peak. Such observations demonstrate the formation of a one-dimensional water-wire in the channels, similar to those observed in other related LAP and PAP chemistries.[7,16] Overall, the internal water-wire structure is seen to be influenced by side-chain length but is only weakly dependent on the ring-size. We will return to this in-channel hydrogen bonding structure later in this article to address the influence of side-chain length on permeability.

To probe the impact of water-channel contacts on water permeability, we enumerate the number of water-channel contacts within a cutoff distance of $r_{\mathrm{HW-channel}} < 0.35$ nm where HW refers to the water-hydrogens.[45] Such hydrogen bond pairing represents the number of contacts a water molecule makes with the surrounding channel and, in turn, represents the frictional effects on the one-dimensional water-wire.

In the insets of Figure 4A,B, we enumerate the number of hydrogen bonds between the water-wire and the channel. We observe an increased number of hydrophilic contacts in LAP6 compared to LAP5. The increase in hydrogen bonding with ring-size is consistent with the addition of two ligands and ring oxygens in LAP6 when compared to LAP5, and the increased contacts reflect the additional hydrophilicity of the LAP6 channel. Comparing the hydrophilic contact results as a function of side-chain length, we observe that the number of hydrogen bonds increases slightly in LAP5 as side-chain length increases ($N_{\mathrm{HBonds}}^{\mathrm{LAP5n4}} = 14.31 \pm 2.36 \rightarrow N_{\mathrm{HBonds}}^{\mathrm{LAP5n8}} = 15.40 \pm 2.68$). In contrast, in LAP6, we observe a more stark increase in hydrogen bonds as side-chain length increases ($N_{\mathrm{HBonds}}^{\mathrm{LAP6n4}} = 16.405 \pm 2.44 \rightarrow N_{\mathrm{HBonds}}^{\mathrm{LAP6n8}} = 18.90 \pm 2.51$). Such results suggest that the role of the side-chains in influencing the permeating water-wire structure is significant in the LAP6 channel by increasing water-channel contacts. With the presence of additional hydrophilic groups in LAP6, one may expect an increase in the number of hydrophilic contacts for larger side-chain lengths. However, the pore size in LAP6 is also expected to be larger than that in LAP5, which would serve to increase the distance between the water-wire and channel walls. Such results suggest that further analysis on the channel structure (Section 4.3) is warranted to understand the origin of increases in hydrophilic contacts.

To summarize, with similar water-wire structures, we observe an increased number of hydrophilic contacts in the LAP6 channel relative to LAP5. This result arises from the addition of hydrophilic groups in the LAP6 ring and is seen to correlate with the reduced water permeabilities with respect to the ring-size in Figure 3. Despite this agreement, the influence of side-chain length on the water−water or water-channel interactions is not consistent with the increases in permeability observed in our simulations. To further understand the role of side-chains, we probe the pore availability, channel structure, hydrogen bonding structure, and channel orientation of our LAP channels.

4.3. Pore Size Availability in LAP5 and LAP6. The observed permeability rates in Figure 3 with respect to ring-size are somewhat counterintuitive since an increase in ring-size is expected to increase the cross-sectional area of the channel. Indeed, it has been reported in earlier works that LAP5 channels have a radius of $r_{\mathrm{LAP5}} = 0.24$ nm, while LAP6 channels have a radius of $r_{\mathrm{LAP6}} = 0.29$ nm.[14] In the previous section, we presented results demonstrating that the additional frictional forces present in LAP6 over LAP5 result in more hydrogen bonding between permeating water molecules and the channel wall. This also contrasts with the expectation that the number of water-wall contacts would decrease in LAP6 due to the theoretically larger pore size. To resolve these observations and also shed further light on the origin of the permeability results, we undertook a more elaborate methodology to probe the pore availability in the channels.

We note that the pore diameters reported in the work by Tan et al. refer to the central quinones that make up the channel's macrocycle.[14] To provide a visualization as to why the pore size distributions may vary so greatly when appended ligands are present, in Figure 5, we present final structures

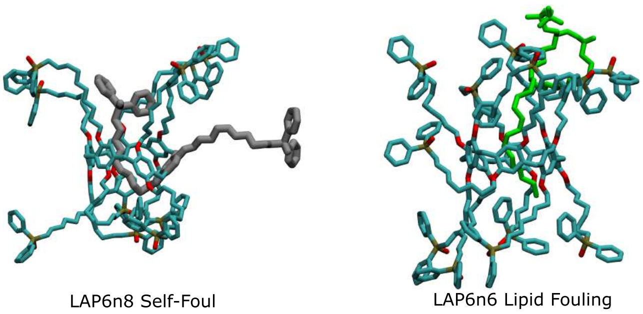

Figure 5. Examples of fouling mechanisms present within the equilibrium simulations wherein (*left*) is a DPP-ligand extending into the channel center, while (*right*) is a lipid molecule that has inserted into the channel.

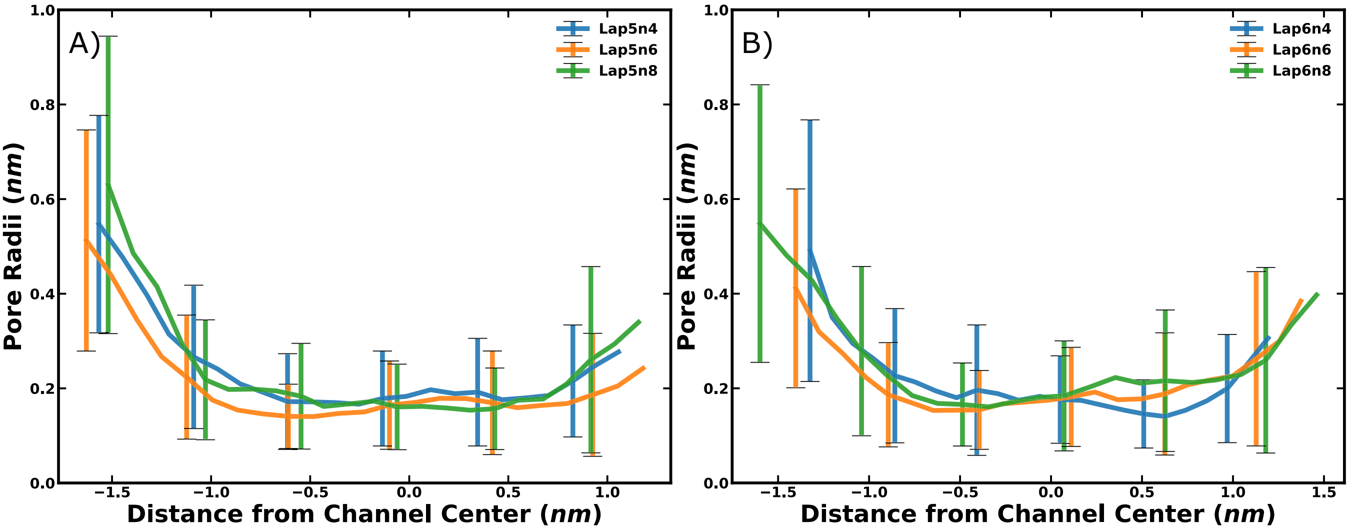

Figure 6. Calculated pore radius profile for (A) LAP5 and (B) LAP6.

Table 1. Average Radii of LAP Channels

channel	$\langle r_{\mathrm{LAP5m}} \rangle$ (nm)	r_{terminal} (nm)	channel	$\langle r_{\mathrm{LAP6m}} \rangle$ (nm)	r_{terminal} (nm)
LAP5n4	0.253 ± 0.172	0.390	LAP6n4	0.202 ± 0.128	0.296
LAP5n6	0.213 ± 0.155	0.336	LAP6n6	0.223 ± 0.153	0.319
LAP5n8	0.248 ± 0.190	0.469	LAP6n8	0.242 ± 0.175	0.348

from our equilibrium simulations and highlight the ligand (gray) and the POPC molecule (green) that are oriented toward the central-axis of the channel. We observe lipid and side-chain partitioning into the central channel pore in our LAP6 channel which appear to foul the channel. Such fouling of channels is expected to lead to a reduction in permeability due to a reduction in free volume in the pore and a reduction in solvent accessible surface area at the bilayer surface. Additionally, such snapshots indicate that these side-chains do not uniformly distribute around the macrocycle and suggest that the population of ligands can change the predicted pore size based on ring-size (m).

Both of the above fouling events are similar in that the aliphatic chains on both the DPP-terminated side-chain and the lipid-tail groups partition into the channel center. We speculate that the mismatch between the hydrophilic ring and hydrophobic side-chain in the LAP6 channel results in a hydrophobic mismatch with the surrounding bilayer, and this leads to a rearrangement of the polar and nonpolar groups in the manner observed in Figure 5.[49] Similar fouling events have been observed in the triphenyl alanine-appended LAP5 molecule in lipid-like block copolymers as well.[19] The presence of these chains along the axis of the channel should lead to a distinct decrease in the channel pore size from the expected radii.

To quantify the pore size distribution along the length of the channel (+z), we use the maximum permeant size approach based on eq 4. Figure 6A,B present the pore size distribution along the channel length for LAP5n(4,6,8) and LAP6n(4,6,8), respectively. Based on the radial profiles shown in Figure 6A,B, the radii near the center of the channel (z = 0.0 nm) are seen to converge to similar radii (r = 0.174 ± 0.02 nm) for both LAP5 and LAP6 channels. This value is lower than the theoretical values suggested for LAP5 and LAP6. Further, from Figure 6A,B, we observe that the center of the channel is a local minima along the radial profile suggesting that the orientation of the channel side-chains generates terminal pore sizes (z = ± 1.0 nm) larger than the central ring-size.

In Table 1, we display the average size of the channel pore and its standard deviation. We observe that the average radii for the LAP5 channel are larger than those calculated for LAP6. LAP5n6 and LAP6n6 are seen to be an exception to this observation; however, these pore sizes differ by only 0.01 nm and suggest that at such similar pore sizes, the additional hydrophilic groups in LAP6n6 will slow a permeating water-wire due to the presence of additional hydrophilic groups.

We observe a monotonic increase in average radii with side-chain length in LAP6 but a nonmonotonic trend in LAP5. Of particular interest, as observed from Table 1, fluctuations in the pore size in the LAP5 channels are, in general, larger than those in LAP6. Hence, we conclude from these results that LAP5 channels provide a larger cross-sectional pore availability on average, contain fewer hydrophilic groups, and form a less rigid pore structure compared with that of LAP6. Under conditions of high packing, previous reports indicate that higher packing factors enhance the observation of dewetting events and that stability of conformation relies on phenyl $\pi-\pi$ stacking.[41] From these observations and comparing them to our results, it appears likely that at high packing factors, LAP6 channels would further exasperate the overcrowding mechanism at the channel interface and display reduced permeabilities compared to LAP5.

The above results help us to conclude that when LAP is appended with DPP-terminated ligands, the additional quinone in the LAP6 macrocycle leads to a net reduction in pore availability compared with LAP5 due to fouling and the presence of side-chains. At such smaller pore sizes, the permeating water-wire is expected to undergo a larger number of hydrophilic contacts with the surrounding channel. These contacts manifest as increased frictional forces on the

https://doi.org/10.1021/acs.jpcb.4c05244
J. Phys. Chem. B 2025, 129, 659−670

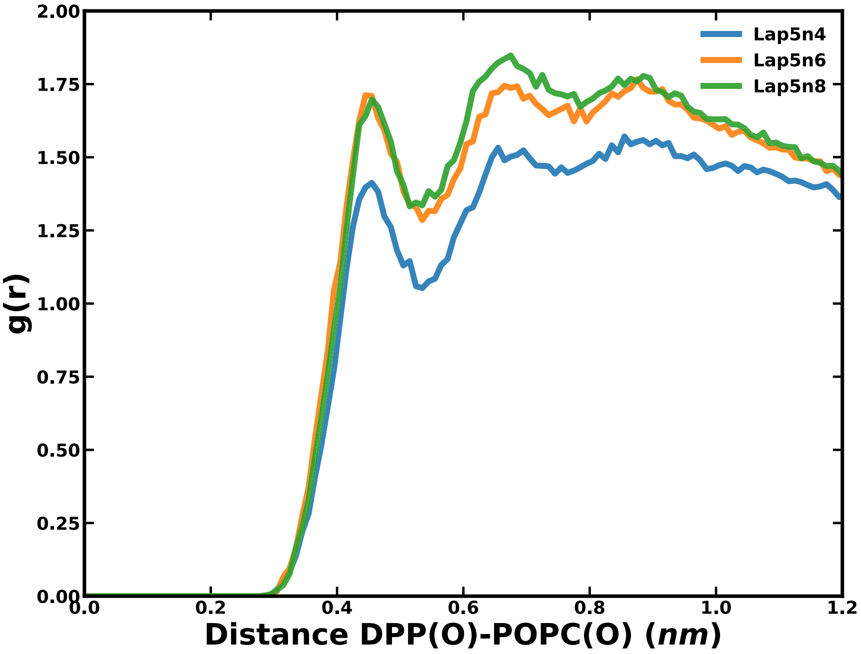

Figure 7. Radial distribution function $g(r)$ between the terminal-DPP oxygen and surrounding phospholipid oxygens in the LAP6 channels.

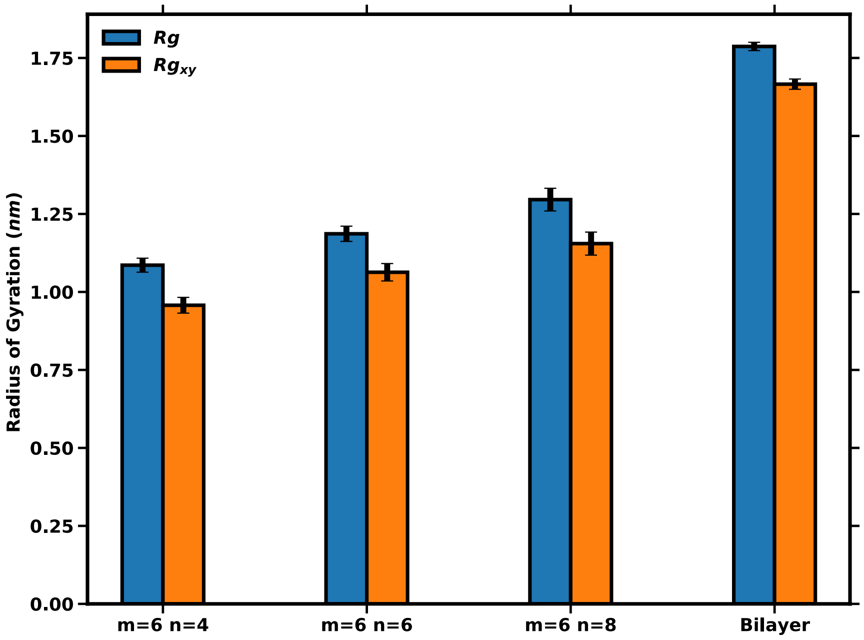

Figure 8. Radius of gyration (R_g), the average extent of the molecule from its center of mass, and its projection in the *xy*-plane for the LAP6 channel molecule. These values are compared to the radius of gyration of the equilibrated POPC bilayer to display the length compatibility between the channel and the surrounding bilayer.

permeating water-wire and would lead to decreased water permeability.[47] Therefore, we conclude that the reduced pore size in the LAP6 channel is the origin of lower permeation of the water-wire compared to that observed in LAP5.

4.4. Effect of Side-Chain Length on LAP6 Permeability. We now turn to the mechanisms underlying the influence of the side-chain length on channel permeability for the LAP6 channels. In the results presented in Figure 3, with increasing side-chain length, we observed a monotonic increase in the water permeability for LAP6 channels. Since our DPP-terminated side-chains do not contain hydrogen bond donating groups along the backbone, our side-chains do not maintain a consistent pore size along the channel length (Figure 4). Indeed, in Table 1, we observe a monotonic increase in the terminal pore size (r_{terminal}) that exceeded the central pore size by 0.1−0.2 nm.[7] This result suggests that the channel structure at the bilayer-water interface likely influences the water permeability in the channel.

The interactions between the terminal-DPP and the surrounding phospholipid heads are characteristic of the change in bilayer compatibility and access to the hydrophilic block. To probe the interactions between the channel terminal-DPP groups and the surrounding hydrophilic heads of the bilayer, we calculated the $g(r)$ between the terminal-DPP

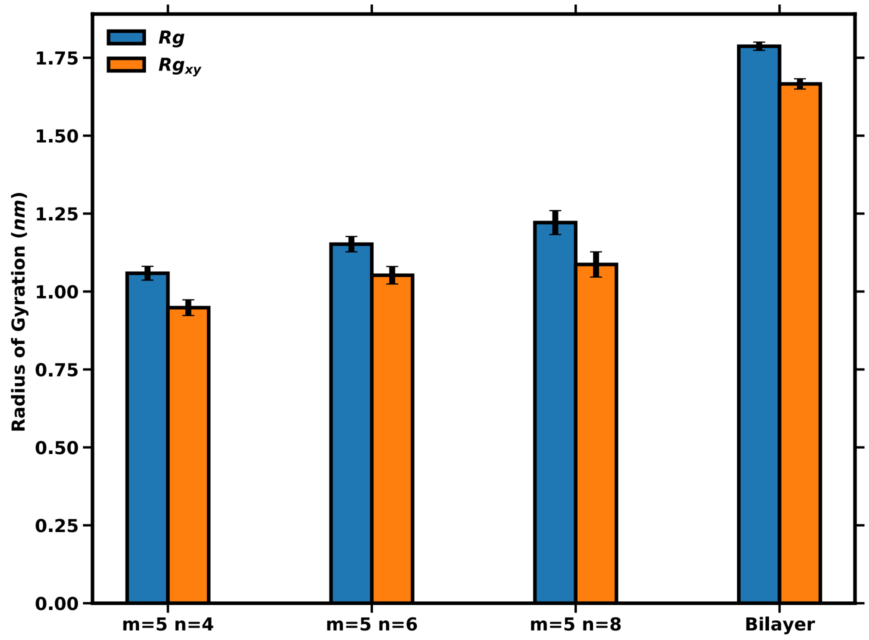

Figure 9. Radius of gyration for the LAP5 channel for side-chain lengths of n = 4, 6, and 8.

oxygen and the phospholipid oxygen. With an increasing side-chain length in Figure 7, we observe a monotonic increase in the $g(r)$ peak intensity between the terminal-DPP oxygens and the surrounding phospholipid heads. This increase in peak intensity corresponds to a higher probability for DPP-terminal groups to interact with the hydrophilic block of the bilayer and enhance pore availability. Additionally, stronger interactions with the bilayer will correspond to more diffuse appended terminal groups in the hydrophilic block, which agrees with our monotonic increase in terminal pore size in Table 1.

We hypothesize that the above increase in bilayer compatibility with side-chain length arises from the role of side-chains in extending the appended ligand terminal groups into the hydrophilic block of the bilayer. To validate this proposal, we calculated the radius of gyration (R_g) as well as the xy projection of R_g to capture the size and distribution of the channel within the bilayer. We present these results for our LAP6 channel parameter space in Figure 8.

In Figure 8, we observe a monotonic increase in R_g and R_{gxy} as the side-chain length increases. The increase in R_{gxy} suggests that as side-chain lengths increase, our side-chains also increase their distribution in the xy-plane. Additionally, we can see that the LAP channels are consistently 0.5−0.7 nm shorter in length than the bilayer length; however, this length mismatch is reduced with increases in side-chain length. This result agrees with our observation in Figure 7 where the $g(r)$ peak intensity increases with side-chain length. The monotonic increase in the R_{gxy} suggests that at longer side-chain lengths, the appended side-chains are able to sample a larger cross-section at the water-bilayer interface and are more likely to make contact with both hydrophilic blocks of the bilayer. We propose that this increased partitioning into the hydrophilic block increases the interfacial pore size with side-chain length and is responsible for the faster water permeation observed in Figure 3.

In summary, the influence of side-chain length in the LAP6 channel increases the water permeability due to stronger interactions between the terminal-DPP groups and the surrounding phospholipid heads. This increased interaction strength is facilitated by the longer channel lengths and wider distributions in the xy-plane. We conclude that such trends with side-chain length lead to monotonic increases in pore size and permeability observed in Figures 3 and 6, respectively.

4.5. Effect of Side-Chain Length on LAP5.

In the previous sections, we rationalized that the higher permeability in LAP5 over that of LAP6 is due to larger pore sizes and reduced hydrophilic contacts. However, in LAP5, we observe a nonmonotonic trend in pore size with side-chain length, which contrasts from the permeability results in Figure 3. To understand the influence of side-chains on the water permeability of the LAP5 channel, we begin by investigating the R_g of the channels as a function of side-chain length.

In Figure 9, we observe a monotonic increase in channel R_g and R_{gxy} as a function of side-chain lengths for LAP5. Similar to the case in LAP6, we observe a length mismatch with the surrounding bilayer of 0.5−0.7 nm that decreases as a function of side-chain length. This suggests that as side-chain length increases, the LAP5 channel terminal groups more effectively access the hydrophilic blocks of the surrounding bilayer. In the results for R_{gxy}, we also observe a large increase in the channel's distribution from LAP5n4 to LAP5n6.

In addition to the R_g of the channel, the alignment of the channel is also expected to influence the access to the hydrophilic blocks and the water permeability. We probed the orientation of the channel in the bilayer through the alignment and bend angle of the channel. The alignment of a channel with the surrounding bilayer determines the degree of hydrophobic mismatch between the bilayer blocks and the channel and is important for channel stability and pore availability at the interface.[12,18] To analyze the alignment of the channel species, we adapted two measures commonly used in the literature.[18] The first is the alignment (θ) of the channel with the membrane normal ($+z$). We define this as the normal vector to the central ring plane, as shown in Figure 2. The second measure is the bend angle (ω) which captures the

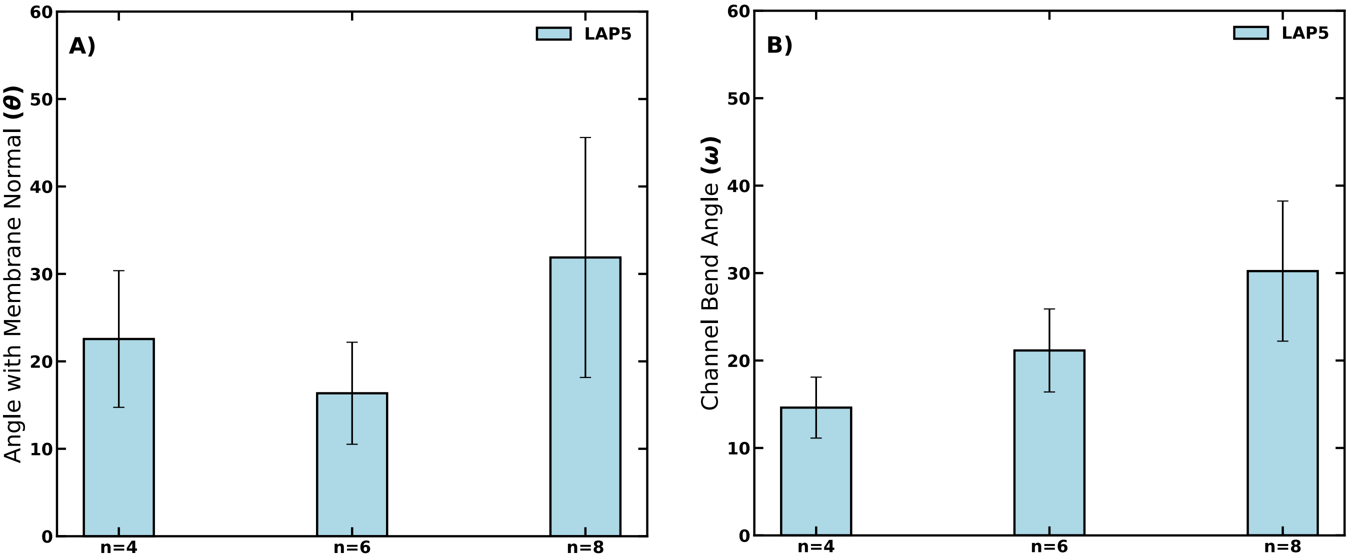

Figure 10. Relative alignment of the LAP5 channel to the bilayer normal (θ) and the channel axis (ω).

relative orientation of the channel side-chains to the central ring.

Figure 10A presents the alignment of each of the LAP channels relative to the bilayer normal (θ) and the channel axis (ω). In Figure 10A, we observe a nonmonotonic trend in the tilt angle as the side-chain length increases. Specifically, we observe that the tilt angle in LAP5n4 is $\theta = 21.32 \pm 8.16°$, while LAP5n6 is seen to exhibit a tilt angle of $\theta = 17.84 \pm 6.93°$. With the high tilt angle in LAP5n4 and smaller R_g, it is expected that the channel terminal groups will be buried further in the surrounding bilayer, thereby forcing water molecules to encounter the hydrophobic region of the bilayer. In contrast, the improved alignment observed in LAP5n6 suggests that the LAP5n6 channel will access each reservoir more directly. Moreover, in Figure 10B, we observe that side-chain lengths, $n = 6$ and $n = 8$, display a bend angle of $\omega = 20.65 \pm 4.69°$ and $\omega = 31.08 \pm 7.93°$, respectively. Such results suggest a compensatory effect between the tilt (θ) and bend (ω) angles where the side-chains compensate well for the misalignment. To contrast, in LAP5n4, we observe a high tilt angle and low bend angle due to shorter side-chain lengths. However, the compensation in LAP5n8 between the tilt and bend angle is expected to enhance the contacts with the bilayer hydrophilic block and lead to an increase in pore size availability over that in LAP5n6, as observed in Figure 6.

We propose that for the LAP5 channels, both the R_g and the alignment of the channel in the bilayer influence the accessibility of the hydrophobic blocks and modulate the water structure and permeation, thereby overcoming the smaller pore sizes observed in LAP5n6 relative to LAP5n4. To further demonstrate the effect of side-chain length on the permeating water-wire and underlying hydrogen bonding structure, we calculated the number of hydrogen bonds each water experiences in the system as a function of the axial coordinate z.[43,44] In Figure 11, we observe that as the water approaches the bilayer interface ($z \approx \pm 2.0$ nm), the water–water hydrogen bonding is reduced at the bilayer-water interface for all side-chain lengths. More interestingly, we observe a nonmonotonic trend in the hydrogen bond disrupted water-wire length as a function of side-chain length. Notably, LAP5n6 displays a slightly longer water-wire length compared to LAP5n8, while LAP5n4's water-wire is shorter compared to LAP5n6 and LAP5n8.

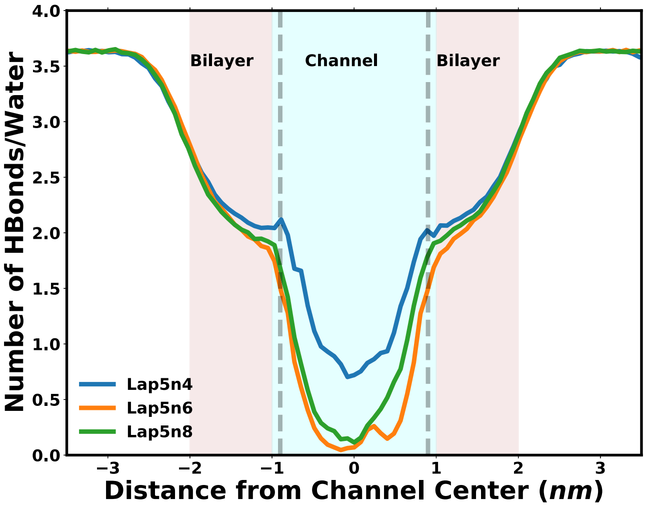

Figure 11. Number of hydrogen bonds per water as a function of distance from the channel center. Shaded regions, bilayer (*light brown*) and channel (*cyan*), indicate the group interacting with water. Vertical lines (*dashed*) represent the interface with the shorter LAP5n4 channel.

Water-wires have shown enhanced dynamics over bulk water in confined environments, and the connectivity and participation of water molecules in the water-wire along the channel length has been shown correlate to the permeability of the channel.[17,50] The region with a reduced number of hydrogen bonds is across a narrower region for the water-wire in LAP5n4 in the z-axial direction observed in Figure 11 and is consistent with the larger tilt angle (θ) and smaller compensatory bend angle (ω) from Figure 10. Particularly, the distance water molecules must travel to form a one-dimensional water in the LAP5n4 channel compared to LAP5n6 suggests that the LAP5n4 channel is recessed in the surrounding hydrophobic block of the bilayer. To contrast, in LAP5n6, the one-dimensional water-wire begins farther from the channel center and more significantly decreases the hydrogen bonding between permeating water-wires. We propose that the longer and less hydrogen bonded water-wire structure seen in LAP5n6 and LAP5n8, arising in turn from the orientation of the channel, is consistent with higher permeabilities observed in such channels compared to the LAP5n4 channel. Between LAP5n6 and LAP5n8, the terminal and overall pore size in LAP5n8 is greater (Figure 6) while also exhibiting similar hydrophilic contacts as those in LAP5n6, which rationalizes the higher permeabilities in LAP5n8.

In summary, the role of side-chain length in LAP5 channels is to increase the length of the internal water-wire and enhance the contacts to either side of the bilayer via an increased bend angle. The bend angle serves as a compensatory effect on the channel tilt angle, which enhances the stability of transmembrane channels and influences the water-wire pathway. The influence of the nonmonotonic pore sizes (Figure 6) is seen to be countered by the strength of the inner water-wire, which results in a monotonic increase in permeability with side-chain lengths in Figure 3.

5. CONCLUSIONS

We presented MD results for the influence of the ring-size and side-chain length on the water permeability of DPP-appended LAP channels. As the ring-size increases, the side-chain orientation leads to a net reduction in pore size and a significant decrease in permeability due to hydrophilic contacts with the permeating water-wire. In LAP6, we demonstrated that increasing the side-chain length results in a monotonic increase in both average pore size and channel length. These trends result in better contact between terminal groups and the hydrophilic block, leading to increased permeability as a function of side-chain length. To contrast, in LAP5, we find that increasing side-chain leads to a nonmonotonic trend in pore size; however, the orientation of the channel extends the length of the permeating water-wire and leads to a monotonic increase in permeability as a function of side-chain length in LAP5.

This study finds that the formation of transmembrane conformations is ubiquitous within DPP-appended LAP chemistries due to strong interactions between the phospholipid heads and DPP terminating groups. The results above suggest that the interfacial characteristics of the LAP channel are a function of the channel compatibility with the surrounding bilayer. Our findings point to further study of LAP5 and LAP4 channels with side-chain lengths that are compatible with the bilayer thickness as a means to increase the LAP permeability. Additionally, the inclusion of hydrogen bonding groups along the channel length will likely provide more control over the pore size and interfacial characteristics.

■ ASSOCIATED CONTENT

Supporting Information

The Supporting Information is available free of charge at https://pubs.acs.org/doi/10.1021/acs.jpcb.4c05244.

> Analysis on a set of channels lacking polar-terminal groups and their resulting conformations within the bilayer; further details on our parametrization, collective diffusion model, and structural calculations for all channels; links to our parameter files and analysis codes; and GROMACS input files for our channels (PDF)
>
> Crystallographic data of channels (MP4)

■ AUTHOR INFORMATION

Corresponding Author

Venkat Ganesan − *McKetta Department of Chemical Engineering, The University of Texas at Austin, Austin, Texas 78712, United States;* orcid.org/0000-0003-3899-5843; Email: venkat@che.utexas.edu

Authors

Tyler J. Duncan − *McKetta Department of Chemical Engineering, The University of Texas at Austin, Austin, Texas 78712, United States*

Harekrushna Behera − *Department of Civil, Architectural and Environmental Engineering, The University of Texas at Austin, Austin, Texas 78712, United States;* orcid.org/0000-0002-8597-5186

Michael F. Meng − *McKetta Department of Chemical Engineering, The University of Texas at Austin, Austin, Texas 78712, United States*

Zidan Zhang − *McKetta Department of Chemical Engineering, The University of Texas at Austin, Austin, Texas 78712, United States;* orcid.org/0000-0002-6909-8742

Nico Marioni − *McKetta Department of Chemical Engineering, The University of Texas at Austin, Austin, Texas 78712, United States;* orcid.org/0009-0001-2307-3064

Meron Tadesse − *McKetta Department of Chemical Engineering, The University of Texas at Austin, Austin, Texas 78712, United States*

Manish Kumar − *McKetta Department of Chemical Engineering and Department of Civil, Architectural and Environmental Engineering, The University of Texas at Austin, Austin, Texas 78712, United States;* orcid.org/0000-0001-5545-3793

Complete contact information is available at: https://pubs.acs.org/10.1021/acs.jpcb.4c05244

Notes

The authors declare no competing financial interest.

■ ACKNOWLEDGMENTS

The authors' work is based upon work supported by the U.S. Department of Energy, Office of Science, Office of Basic Energy Sciences, under Award #DE-SC0023265. Zidan Zhang, supported by grants from Robert A. Welch Foundation (F1599), and Meron Tadesse, by National Science Foundation (DMR-2225167), contributed through discussions related to unimolecular channels. Nico Marioni, supported by by the Center for Materials for Water and Energy Systems, an Energy Frontier Research Center funded by the U.S. Department of Energy, Office of Science, Basic Energy Sciences under Award #DE-SC0019272, contributed to the development of hydrogen bond analyses. The authors acknowledge the Texas Advanced Computing Center (TACC) for the generous allocation of computing resources.

■ REFERENCES

(1) Panagopoulos, A. *Environmental Science and Pollution Research* **2021**, *28*, 21009−21022.

(2) Mezher, T.; Fath, H.; Abbas, Z.; Khaled, A. *Desalination* **2011**, *266*, 263−273.

(3) Kimani, E.; Pranić, M.; Porada, S.; Kemperman, A.; Ryzhkov, I.; Van Der Meer, W.; Biesheuvel, P. *J. Membr. Sci.* **2022**, *660*, No. 120800.

(4) Liu, L.; Chen, X.; Feng, S.; Wan, Y.; Luo, J. *ACS Appl. Mater. Interfaces* **2022**, *14*, 36132−36142.
(5) Song, N.; Yang, Y.-W. *Science China Chemistry* **2014**, *57*, 1185−1198.
(6) Kumar, M.; Grzelakowski, M.; Zilles, J.; Clark, M.; Meier, W. *Proc. Natl. Acad. Sci. U. S. A.* **2007**, *104*, 20719−20724.
(7) Shen, Y.-X.; Song, W.; Barden, D. R.; Ren, T.; Lang, C.; Feroz, H.; Henderson, C. B.; Saboe, P. O.; Tsai, D.; Yan, H.; et al. *Nat. Commun.* **2018**, *9*, 2294.
(8) Cai, K.; Zhou, X.; Shi, J.; Qin, Q.-H. *Microfluid. Nanofluid.* **2022**, *26*, 91.
(9) Hashido, M.; Ikeguchi, M.; Kidera, A. *FEBS Lett.* **2005**, *579*, 5549−5552.
(10) Li, Y.; Li, Z.; Aydin, F.; Quan, J.; Chen, X.; Yao, Y.-C.; Zhan, C.; Chen, Y.; Pham, T. A.; Noy, A. *Sci. Adv.* **2020**, *6*, No. eaba9966.
(11) Tunuguntla, R. H.; Henley, R. Y.; Yao, Y.-C.; Pham, T. A.; Wanunu, M.; Noy, A. *Science* **2017**, *357*, 792−796.
(12) Shen, C.; Zou, G.; Guo, W.; Gao, H. *Carbon* **2020**, *164*, 391−397.
(13) Kali, R.; Milner, S. T. *Molecular Systems Design & Engineering* **2022**, *7*, 273−284.
(14) Tan, L.-L.; Yang, Y.-W. *Journal of Inclusion Phenomena and Macrocyclic Chemistry* **2015**, *81*, 13−33.
(15) Yan, Z.-J.; Wang, D.; Ye, Z.; Fan, T.; Wu, G.; Deng, L.; Yang, L.; Li, B.; Liu, J.; Ma, T.; et al. *J. Am. Chem. Soc.* **2020**, *142*, 15638−15643.
(16) Chen, L.; Wang, Y.; Yuan, X.; Ren, Y.; Liu, N.; Yuan, L.; Feng, W. *Sep. Purif. Technol.* **2018**, *192*, 152−159.
(17) Song, W.; Joshi, H.; Chowdhury, R.; Najem, J. S.; Shen, Y.-X.; Lang, C.; Henderson, C. B.; Tu, Y.-M.; Farell, M.; Pitz, M. E.; et al. *Nat. Nanotechnol.* **2020**, *15*, 73−79.
(18) Allen, T. W.; Andersen, O. S.; Roux, B. *J. Am. Chem. Soc.* **2003**, *125*, 9868−9877.
(19) Kali, R.; Andini, E.; Milner, S. T. *J. Membr. Sci.* **2021**, *630*, No. 119279.
(20) Dam, H. H.; Reinhoudt, D. N.; Verboom, W. *Chem. Soc. Rev.* **2007**, *36*, 367−377.
(21) Waldman, R. Z.; Gao, F.; Phillip, W. A.; Darling, S. B. *J. Membr. Sci.* **2021**, *633*, No. 119389.
(22) Zhu, F.; Tajkhorshid, E.; Schulten, K. *Phys. Rev. Lett.* **2004**, *93*, No. 224501.
(23) Abraham, M. J.; Murtola, T.; Schulz, R.; Páll, S.; Smith, J. C.; Hess, B.; Lindahl, E. *SoftwareX* **2015**, *1−2*, 19−25.
(24) Berendsen, H. J. C.; Grigera, J. R.; Straatsma, T. P. *J. Phys. Chem.* **1987**, *91*, 6269−6271.
(25) Moore, P. B.; Lopez, C. F.; Klein, M. L. *Biophys. J.* **2001**, *81*, 2484−2494.
(26) Kulig, W.; Pasenkiewicz-Gierula, M.; Róg, T. *Data in Brief* **2015**, *5*, 333−336.
(27) Kulig, W.; Pasenkiewicz-Gierula, M.; Róg, T. *Chem. Phys. Lipids* **2016**, *195*, 12−20.
(28) Maciejewski, A.; Pasenkiewicz-Gierula, M.; Cramariuc, O.; Vattulainen, I.; Rog, T. *J. Phys. Chem. B* **2014**, *118*, 4571−4581.
(29) Dodda, L. S.; Cabeza de Vaca, I.; Tirado-Rives, J.; Jorgensen, W. L. *Nucleic Acids Res.* **2017**, *45*, W331−W336.
(30) Robertson, M. J.; Skiniotis, G. *J. Chem. Theory Comput.* **2022**, *18*, 4482−4489.
(31) Guvench, O.; MacKerell, A. D. *Molecular Modeling of Proteins*, Kukol, A., Ed.; Humana Press: Totowa, NJ, 2008; pp. 63−88.
(32) Robertson, M. J.; Tirado-Rives, J.; Jorgensen, W. L. *J. Chem. Theory Comput.* **2015**, *11*, 3499−3509.
(33) Kaminski, G. A.; Friesner, R. A.; Tirado-Rives, J.; Jorgensen, W. L. *J. Phys. Chem. B* **2001**, *105*, 6474−6487.
(34) Hanwell, M. D.; Curtis, D. E.; Lonie, D. C.; Vandermeersch, T.; Zurek, E.; Hutchison, G. R. *J. Cheminform.* **2012**, *4*, 17.
(35) Ribeiro, A. A. S. T.; Horta, B. A. C.; Alencastro, R. B. D. *J. Braz. Chem. Soc.* **2008**, *19*, 1433−1435.
(36) Wang, J.; Cieplak, P.; Kollman, P. A. *J. Comput. Chem.* **2000**, *21*, 1049−1074.
(37) Frisch, M.; Trucks, G.; Schlegel, H. B.; Scuseria, G.; Robb, M.; Cheeseman, J.; Scalmani, G.; Barone, V.; Petersson, G.; Nakatsuji, H. et al. *Gaussian 16*, https://gaussian.com/ (accessed 05/03/2022).
(38) Lemkul, J. *MD Tutorials Publication Title*: MDTutorials.com, http://www.mdtutorials.com/ (accessed 06/01/2022).
(39) Hess, B.; Bekker, H.; Berendsen, H. J. C.; Fraaije, J. G. E. M. *J. Comput. Chem.* **1997**, *18*, 1463−1472.
(40) Shen, Y.-X.; Si, W.; Erbakan, M.; Decker, K.; De Zorzi, R.; Saboe, P. O.; Kang, Y. J.; Majd, S.; Butler, P. J.; Walz, T.; et al. *Proc. Natl. Acad. Sci. U. S. A.* **2015**, *112*, 9810−9815.
(41) Liu, Y.; Vashisth, H. *Phys. Chem. Chem. Phys.* **2019**, *21*, 22711−22721.
(42) Tieleman, D. P.; Berendsen, H. J. C. *J. Chem. Phys.* **1996**, *105*, 4871−4880.
(43) Michaud-Agrawal, N.; Denning, E. J.; Woolf, T. B.; Beckstein, O. *J. Comput. Chem.* **2011**, *32*, 2319−2327.
(44) Gowers, R. J.; Linke, M.; Barnoud, J.; Reddy, T. J. E.; Melo, M. N.; Seyler, S. L.; Domański, J.; Dotson, D. L.; Buchoux, S.; Kenney, I. M. et al. *Proceedings of the 15th Python in Science Conference*, 2016, pp. 98−105.
(45) Taylor, R.; Kennard, O.; Versichel, W. *Acta Crystallographica Section B-structural Science* **1984**, *40*, 280−288.
(46) Frallicciardi, J.; Gabba, M.; Poolman, B. *Nat. Protoc.* **2022**, *17*, 2620−2646.
(47) Qiu, Z.; Chen, J.; Zeng, J.; Dai, R.; Wang, Z. *Water Res.* **2023**, *247*, No. 120774.
(48) Ohba, T.; Kaneko, K.; Endo, M.; Hata, K.; Kanoh, H. *Langmuir* **2013**, *29*, 1077−1082.
(49) Killian, J. *Biochimica et Biophysica Acta (BBA) - Reviews on Biomembranes* **1998**, *1376*, 401−416.
(50) Barden, D. R.; Vashisth, H. *Front. Chem.* **2021**, *9*, No. 753635.